ARTICLES
PUBLISHED ONLINE: 2 MAY 2010 | DOI: 10.1038/NNANO.2010.84

nature nanotechnology

Hybrid superconductor–semiconductor devices made from self-assembled SiGe nanocrystals on silicon

G. Katsaros[1]*, P. Spathis[1], M. Stoffel[2], F. Fournel[3], M. Mongillo[1], V. Bouchiat[4], F. Lefloch[1], A. Rastelli[2], O. G. Schmidt[2] and S. De Franceschi[1]*

The epitaxial growth of germanium on silicon leads to the self-assembly of SiGe nanocrystals by a process that allows the size, composition and position of the nanocrystals to be controlled. This level of control, combined with an inherent compatibility with silicon technology, could prove useful in nanoelectronic applications. Here, we report the confinement of holes in quantum-dot devices made by directly contacting individual SiGe nanocrystals with aluminium electrodes, and the production of hybrid superconductor–semiconductor devices, such as resonant supercurrent transistors, when the quantum dot is strongly coupled to the electrodes. Charge transport measurements on weakly coupled quantum dots reveal discrete energy spectra, with the confined hole states displaying anisotropic gyromagnetic factors and strong spin–orbit coupling with pronounced dependences on gate voltage and magnetic field.

The bottom-up fabrication of electronic devices from predefined nanoscale structures is a major theme in nanoelectronics, and different types of nanostructures have been considered as potential building blocks for such devices. Carbon nanotubes and semiconductor nanowires, for example, have been used to fabricate high-performance field-effect transistors and basic functional circuits[1–4]. Although these achievements represent important steps towards low-cost electronics, there are challenges to overcome with respect to integration with mainstream silicon technology and scaling to high-density electronic circuits with large numbers of interconnected devices.

Here, we propose a new approach to bottom-up nanodevices based on self-assembled silicon–germanium (SiGe) nanocrystals grown directly on silicon by molecular-beam epitaxy by means of the so-called Stranski–Krastanow growth mode[5,6]. These nanocrystals can have a variety of sizes and shapes (Fig. 1a)[7,8], and their composition can be controlled to a high degree by adjusting the growth parameters[9]. In addition, their positions can be controlled by prepatterning the growth surface (Fig. 1a)[10,11]. However, despite being potentially scalable and compatible with CMOS technology[12], there have been no reports of practical devices based on self-assembled SiGe nanocrystals to date.

Another advantage of SiGe nanostructures is their ability to form ideal contacts with metals, which is essential for making hybrid superconductor–semiconductor devices, as demonstrated in the recent observation of a gate-tunable supercurrent (of holes) in Ge/Si core–shell nanowires[13]. Here, we take advantage of the smaller contact area and lower dimensionality of self-assembled SiGe nanocrystals to extend gate control of the supercurrent to the single-hole level.

SiGe nanostructures could also have applications in semiconductor spintronics because of their potential for long spin coherence times[14–18]. Although both n- and p-type structures have been studied recently, the p-type structures are of additional interest mainly because of the stronger spin–orbit (SO) coupling of the valence-band states. SO coupling can induce large modulations and anisotropies in the Landé g-factor[19–22], enabling electrically controlled spin precession[23]. To date, experimental efforts have focused on coupled quantum-dot systems (created by local electrostatic gating in p-type Ge/Si core–shell nanowires)[14], and indirect evidence for SO coupling has been found in the g-factor of weakly confined hole states[24]. The quantum-dot devices made from self-assembled SiGe nanocrystals demonstrated here show more pronounced SO effects in the strong quantum confinement regime, and spin-1/2 hole states with largely anisotropic g-factors when the quantum dot contains an odd number of holes. In addition to spintronics, self-assembled SiGe nanocrystals may facilitate the development of two-dimensional qubit architectures in quantum information applications, as opposed to one-dimensional architectures based on Ge/Si core–shell nanowires.

Inspired by recent work on self-assembled InAs nanocrystals[25–27], we have developed a nanolithographic process to laterally contact pairs of 20-nm-thick aluminium electrodes (to be used as source and drain electrodes) with single self-assembled SiGe nanocrystals. Although SiGe and InAs nanocrystals have similar shapes and sizes, InAs nanocrystals are grown on GaAs rather than silicon and, when connected to metal electrodes, they confine electrons rather than holes. Devices made from InAs nanocrystals can be gated by growing the nanocrystals on heavily-doped GaAs-based heterostructures[25–27]. Here, to add gate control, the SiGe nanocrystals were grown on silicon-on-insulator (SOI) substrates consisting of an undoped silicon overlayer, a SiO_2 insulating layer, and a degenerately doped silicon substrate that was used as a back-gate (see Supplementary Information). We focused on SiGe nanocrystals that had a characteristic dome-like shape, with a height of ~20 nm and a base diameter of ~80 nm, a 2-nm-thick silicon capping layer, and a band structure that confines holes (Fig. 1b). At room temperature, the upper silicon layer of the SOI substrate introduces a significant parallel conduction path. Below ~100 K, however,

[1]CEA, INAC/SPSMS/LaTEQS, 17 Rue des Martyrs, 38054 Grenoble, France, [2]IFW-Dresden, Institute for Integrative Nanosciences, Helmholtzstrasse 20, 01069 Dresden, Germany, [3]CEA, LETI, MINATEC, F38054 Grenoble, France, [4]Institut Néel, CNRS and Université Joseph Fourier, BP 166, 38042 Grenoble cedex 9, France. *e-mail: georgios.katsaros@cea.fr; silvano.defranceschi@cea.fr

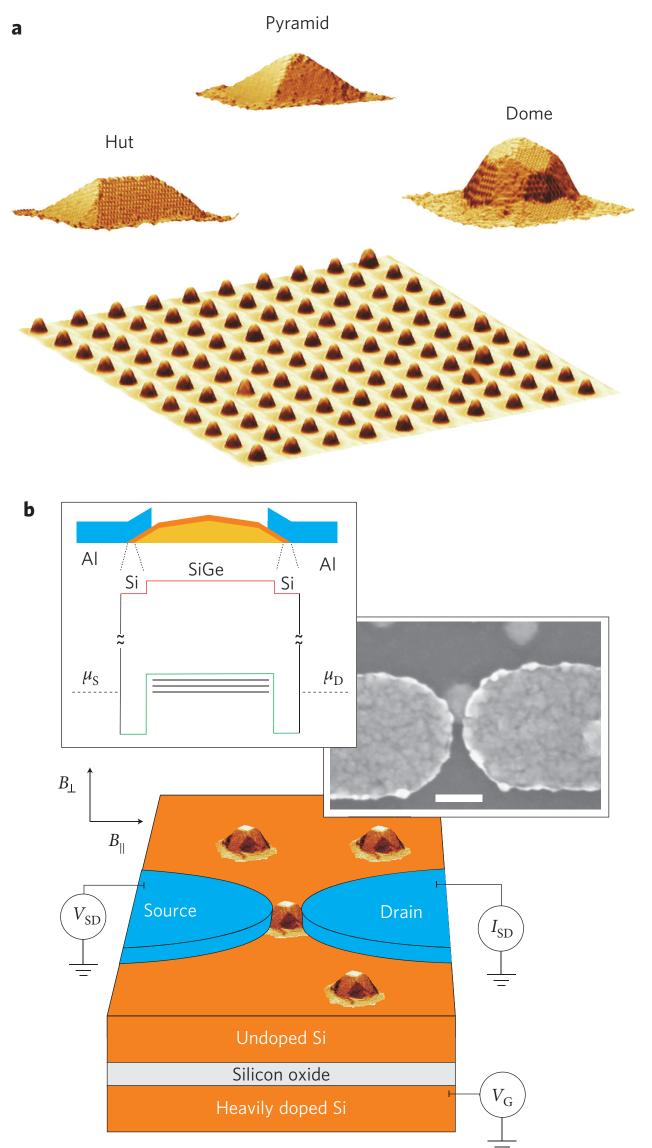

Figure 1 | Structure and growth of SiGe self-assembled nanocrystals and device layout. a, Top: three-dimensional scanning tunnelling micrographs of self-assembled SiGe nanocrystals with characteristic 'hut', 'pyramid' and 'dome' shapes. The corresponding dimensions are $50 \times 32 \times 7$ nm^3, $50 \times 32 \times 7$ nm^3 and $50 \times 50 \times 10$ nm^3, respectively. These sizes can be tuned by adjusting the growth conditions. For the present work we used dome-shaped monocrystals with a height of ~20 nm and a base diameter of ~80 nm. Bottom: atomic-force micrograph (4.7×4.7 μm^2) illustrating an example of a self-organized array of SiGe nanocrystals grown on a prepatterned silicon wafer. **b**, Bottom panel: schematic of a quantum-dot device obtained by contacting a single SiGe nanocrystal to aluminium source/drain electrodes. The heavily doped substrate is used as a back-gate. Middle-right panel: scanning-electron micrograph of a representative device. Scale bar, 100 nm. Top-left panel: schematic cross-section of a device and the associated valence band (green line) and conduction band (red). The SiGe nanocrystal, which is covered by a 2-nm-thick silicon layer, acts as a confining potential for holes (quantized levels schematically shown as a set of black horizontal lines). The valence-band edge lies close to the Fermi energies, μ_S and μ_D, of the source and drain electrodes. This band alignment is consistent with that given in ref. 2 for germanium/silicon core–shell nanowires.

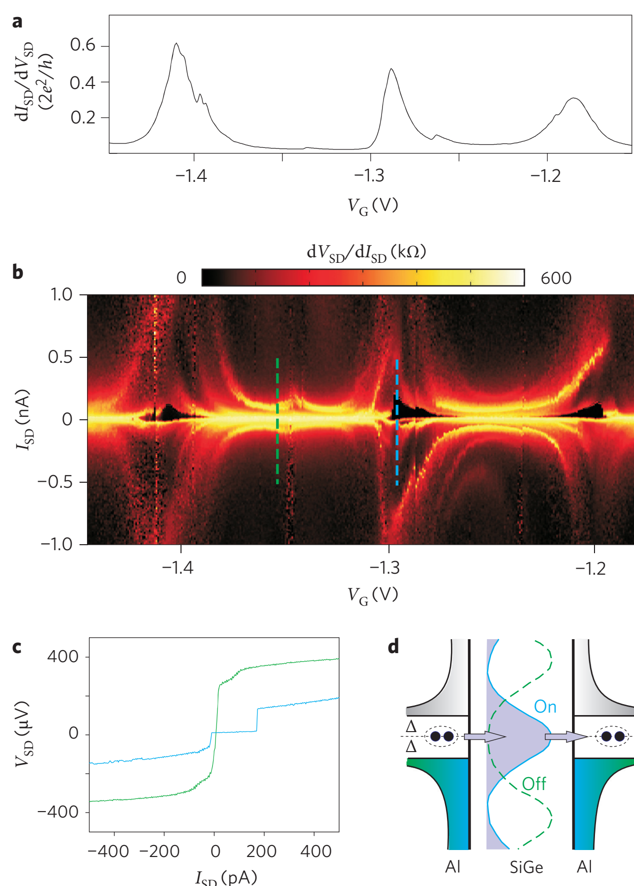

Figure 2 | SiGe single-hole supercurrent transistor. a, Zero-bias differential conductance, dI_{SD}/dV_{SD}, versus back-gate voltage, V_G, showing Coulomb-blockade oscillations in a low-impedance device at 15 mK, with a 75-mT perpendicular magnetic field suppressing superconductivity in the aluminium electrodes. **b**, False-colour plot of the differential resistance, dV_{SD}/dI_{SD}, as a function of V_G and I_{SD}. In the absence of an applied magnetic field the aluminium electrodes are superconducting. Resonant supercurrents can be clearly observed as black regions at the position of the charge degeneracy points. The bright regions between indicate the Coulomb blockade regime. **c**, Representative $V_{SD}(I_{SD})$ traces extracted from **b** at the blue and green vertical lines, illustrating the device behaviour on (blue) and off (green) resonance. A series resistance of ~40 kΩ corresponding to low-temperature low-pass filters, wiring and measurement electronics has been substracted in both **b** and **c. d**, Qualitative electronic density of states (horizontal axis) versus energy (vertical axis) for a SiGe quantum dot between aluminium superconducting leads. In the leads, an energy gap Δ separates the condensate of Cooper pairs at the Fermi energy from occupied and unoccupied single-particle states. In the quantum dot, the discrete hole levels are shown as peaks with a lifetime broadening due to tunnelling. The gate voltage tunes the energy of the quantum-dot levels with respect to the Fermi energy of the leads. Because Cooper pair tunnelling takes place on resonance (blue line) and is suppressed off resonance (green dashed line), the device can be electrically switched from superconducting to dissipative states by a small change in V_G.

transport occurs uniquely by holes tunnelling from the source to the drain via the SiGe quantum dot. All of the measurements on an ensemble of 12 similar devices were taken at 15 mK. We found characteristic device resistances between $\sim 1 \times 10^4$ and $\sim 1 \times 10^5$ Ω. The lowest values are close to the quantum resistance, $h/e^2 = 25.8$ kΩ, denoting high contact transparency.

Single-hole supercurrent transistor

At 15 mK the aluminium electrodes are superconducting, but they can be turned into normal-type electrodes by applying a perpendicular magnetic field, $B_\perp$, of a few tens of millitesla. The differential

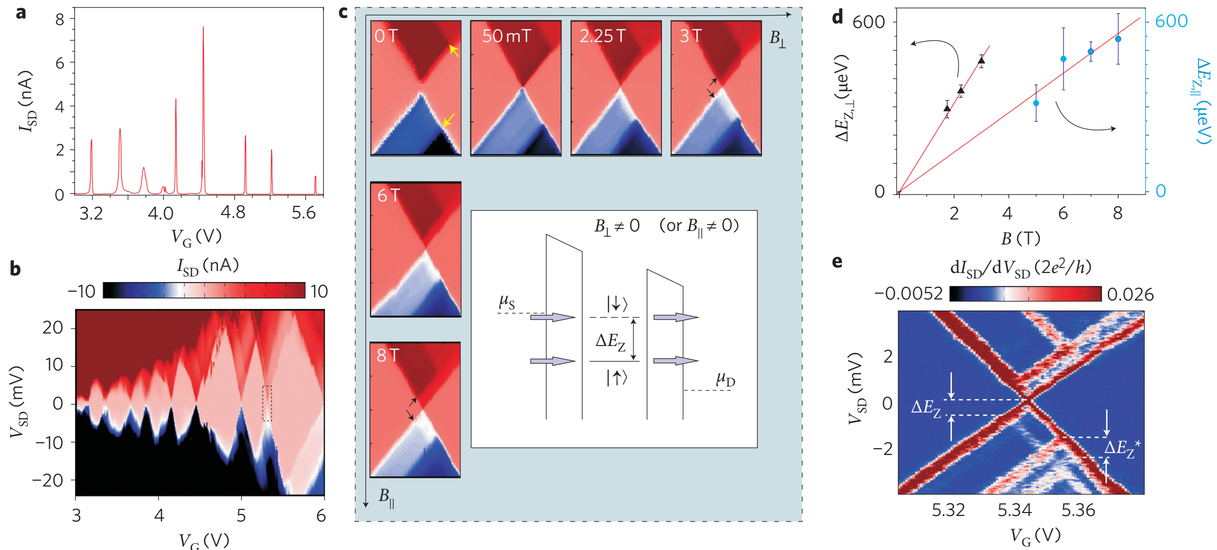

Figure 3 | Tunnelling spectroscopy measurements on a high-resistance device. **a**, Representative Coulomb-blockade oscillations in a plot of I_{SD} versus V_G at 15 mK and $V_{SD} = 1$ mV. **b**, False-colour plot of I_{SD} as a function of V_G and V_{SD}, with a 50-mT perpendicular magnetic field suppressing superconductivity in the contacts. **c**, False-colour plots of I_{SD} as a function of V_G and V_{SD} for different parallel and perpendicular magnetic fields. V_{SD} spans an 8-mV range around zero bias, and V_G a 100-mV range around the charge degeneracy point (which corresponds to the dotted rectangle in **b**). The yellow arrows indicate the onset of single-hole tunnelling via an excited orbital state. Finite parallel or perpendicular magnetic fields cause the edges of the right Coulomb diamond to split due to lifted degeneracy in the spin-1/2 ground state of the left diamond. The black arrows indicate the onset of single-hole tunnelling via the spin-down ($|\downarrow\rangle$) excited state as represented by the energy diagram in the inset. (Because SiGe nanocrystals consist mainly of germanium, hole g-factors are likely negative. Hence $|\uparrow\rangle$ and $|\downarrow\rangle$ correspond to spin parallel and antiparallel to the applied field, respectively.) The Zeeman splitting, ΔE_Z, between $|\uparrow\rangle$ and $|\downarrow\rangle$ states can be extracted from the splitting of the corresponding diamond edges. **d**, ΔE_Z versus parallel magnetic field (right axis) or perpendicular magnetic field (left axis) as extracted from **c** and similar measurements. For each field, ΔE_Z is obtained after averaging over different V_G values and error bars are determined by the resulting standard deviation. Solid lines are fits to a linear dependence: $\Delta E_Z = g\mu_B B$. Anisotropy between parallel and perpendicular g-factors is observed. **e**, False-colour plot of dI_{SD}/dV_{SD} as a function of V_G and V_{SD} for an 8-T parallel field. Zeeman splitting is observed for ground and excited orbital states, yielding ΔE_Z and ΔE_Z^*, respectively.

conductance, dI_{SD}/dV_{SD}, of a low-resistance device is shown in Fig. 2a as a function of back-gate voltage, V_G, at $B_\perp = 75$ mT. The observed oscillations are a consequence of the on-site Coulomb interaction forcing holes to tunnel one by one across the SiGe quantum dot. The conductance valleys correspond to the Coulomb blockade regime in which the quantum dot hosts an integer number of confined holes. Each conductance peak corresponds to an energy degeneracy between consecutive charge states. The large width of the Coulomb peaks and the finite valley conductance indicate a strong tunnel coupling to the source and drain leads. As the contact electrodes are turned into a superconducting state by removing the magnetic field, this strong coupling enables the onset of Cooper pair tunnelling across the quantum dot, leading to measurable supercurrents[28–33].

This non-dissipative transport mechanism is modulated by the gate voltage, as can be seen from current-biased measurements (Fig. 2b). The measured voltage drop across the SiGe quantum dot is suppressed around the charge degeneracy points, indicating resonant supercurrent transport. A representative $V_{SD}(I_{SD})$ trace taken at a Coulomb-blockade resonance is given in Fig. 2c. The device switches from superconducting to dissipative regimes at a bias current of $\sim 1 \times 10^2$ pA. No supercurrent branch is observed in the adjacent Coulomb valley (green dashed line in Fig. 2b), as shown by the representative green trace in Fig. 2c. As a result, at low current bias the device can be turned from a superconducting 'on' state to a dissipative 'off' state by a small change in the gate voltage (which corresponds to a fractional variation of the device charge; Fig. 2d).

Tunable hole spin states

We now consider the opposite case of a high-resistance device and focus on the spin-dependent properties of self-assembled SiGe quantum dots. In the normal state ($B_\perp = 50$ mT), well-separated Coulomb blockade resonances are observed in a measurement of I_{SD} versus V_G (Fig. 3a), with device conductance vanishing in the Coulomb valleys. Additional information is obtained by plotting I_{SD} versus (V_G,V_{SD}) as shown in Fig. 3b. The Coulomb blockade regime occurs within the regions with the characteristic diamond shape. On average, the diamond size grows from left to right, indicating an increase of the charging energy from $\sim$5 to $\sim$20 meV (caused mainly by a decrease in the tunnel and capacitive coupling between the quantum dot and the leads).

By zooming into the rightmost charge degeneracy point in Fig. 3b, additional features become visible (Fig. 3c). At zero field, the Coulomb diamonds are slightly split apart along the V_{SD} axis, leading to the appearance of a 'currentless window' around zero bias. This feature arises due to the superconducting gap in the quasiparticle density of states of the electrodes (Cooper pair tunnelling and sub-gap transport are suppressed for high tunnel resistances). A second important feature is the presence of additional current steps, appearing as lines parallel to the diamond edges (see yellow arrows in Fig. 3c). These steps arise from single-hole tunnelling via higher-energy orbital levels, demonstrating that SiGe nanocrystals form true quantum dots with discrete energy spectra.

At finite perpendicular fields, Zeeman spin splitting of the discrete quantum dot levels is revealed by the appearance of new excitation lines such as those indicated by black arrows in Fig. 3c. A similar behaviour is seen for fields parallel to the substrate. The observed twofold splitting of the right-diamond edges denotes a ground state with spin $S = 1/2$ in the left-diamond. The absolute value of the g-factor of the hole can be extracted from the magnitude of the Zeeman splitting, $\Delta E_Z = g\mu_B B$, where μ_B is the Bohr magneton (Figs 3c–e). The measured g-factors differ substantially from the

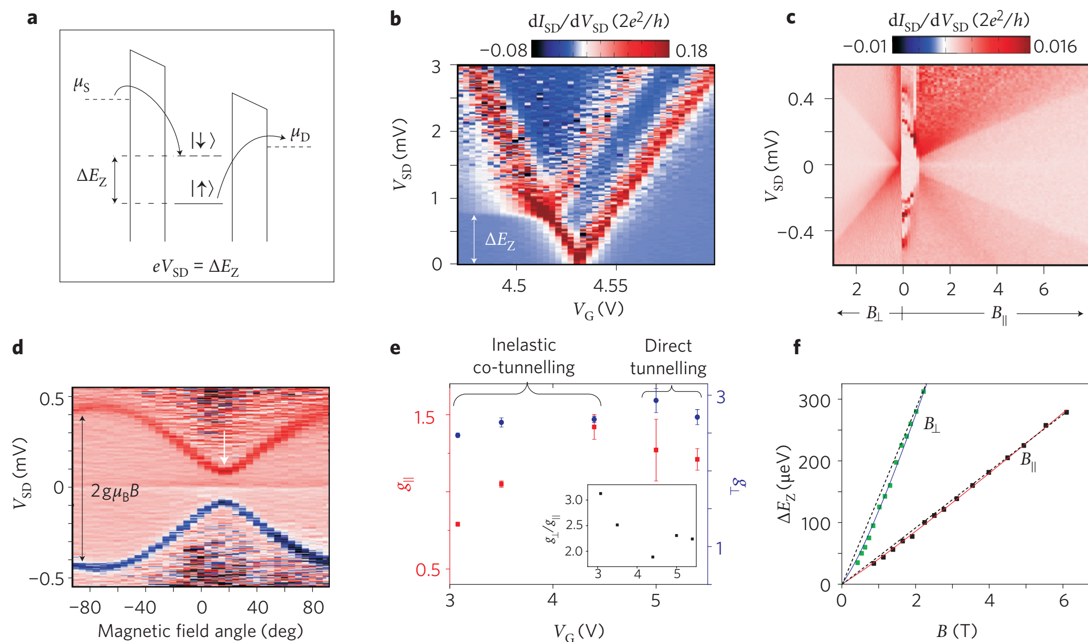

Figure 4 | Anisotropy and gate dependence of the hole g-factors. a, Schematic energy diagram showing the onset condition ($eV_{SD} = \Delta E_Z$) for spin-flip inelastic co-tunnelling. **b**, False-colour plot of dI_{SD}/dV_{SD} as a function of V_G and V_{SD} for a parallel magnetic field of 8 T. The Zeeman splitting (ΔE_Z) of the spin-1/2 ground state in the left Coulomb diamond can be accurately measured from the value of V_{SD} at which there is a step change in dI_{SD}/dV_{SD} due to inelastic spin-flip co-tunnelling. **c**, False-colour plot of dI_{SD}/dV_{SD} as a function of magnetic field and V_{SD}; $V_G = 3.52$ V. The position of the inelastic co-tunnelling step varies with the strength of the magnetic field (both perpendicular and parallel). **d**, The position of the inelastic co-tunnelling step also varies with the angle of the magnetic field (3 T in this plot) with respect to the parallel direction; $V_G = 3.1$ V. The position of the minimum splitting (white arrow) does not correspond to the parallel direction. As a result, the minimum g-factor, $g_{min} \approx 0.5$, is significantly smaller than the zero-angle g-factor, $g_\parallel \approx 0.8$, and the maximum anisotropy, $g_{max}/g_{min} \approx 5$, is consequently larger than $g_\perp/g_\parallel \approx 3.1$. **e**, Absolute values of the parallel and perpendicular g-factors measured on the same device at different V_G. For a better comparison between the g-factor values extracted from direct-tunnelling data and from co-tunnelling data, linear fits were always taken in the large magnetic-field range. Inset: plot of the g-factor anisotropy versus V_G. **f**, Plot of Zeeman splitting (measured from the inelastic co-tunnelling spectroscopy) for parallel and perpendicular magnetic fields; $V_G = 3.1$ V. The dashed lines are linear fits at high magnetic fields; the extracted values are the ones reported in Fig. 4e. The g-factors exhibit an appreciable nonlinearity when plotted over the full range of magnetic field values: however, they can be fitted to a power-law: $\Delta E_Z \approx 2.06\ \mu_B B_\perp^{1.2}$ for perpendicular fields, and $\Delta E_Z \approx 0.71\ \mu_B B_\parallel^{1.07}$ for parallel fields.

free-electron value (2.002) and exhibit a pronounced anisotropy, with $g_\perp = 2.71$ and $g_\parallel = 1.21$ being the perpendicular- and parallel-field values, respectively. This anisotropy is qualitatively consistent with recent calculations for pure germanium islands with pyramidal shape[34]. Similar anisotropies have also been reported for strained bulk germanium[35], acceptor levels in silicon/germanium/silicon heterostructures[36] and germanium/silicon core–shell nanowires[24].

To investigate the dependence of the g-factor on the number of confined holes, we have carried out similar measurements for other charge degeneracy points in the V_G range of Fig. 3b. We find an alternation of $S = 0$ and $S = 1/2$ ground states, corresponding to an even and odd filling of spin-degenerate levels, respectively. As noticed above, lowering V_G leads to a larger tunnel coupling between the SiGe quantum dot and the metal contacts, resulting in a larger energy broadening, Γ, of the quantum dot levels. Because the resolution of single-hole tunnelling spectroscopy is limited by Γ, the experimental uncertainty on ΔE_Z increases. At sufficiently large tunnel coupling, however, two-electron processes begin to contribute a measurable current in the Coulomb blockade regime, providing a powerful spectroscopy tool. In fact co-tunnelling processes can induce internal excitations at finite bias. The onset of these so-called 'inelastic' processes occurs when eV_{SD} equals the energy needed to create an excitation in the quantum dot, leading to a step-like increase in dI_{SD}/dV_{SD} (see Fig. 4a). The step width is uniquely determined by the electronic temperature, resulting in a high resolution at low temperatures[37].

This is clearly seen in Fig. 4b, where dI_{SD}/dV_{SD} is plotted as a function of (V_G,V_{SD}) around a charge degeneracy point and for $B_\parallel = 8$ T. The Zeeman splitting is simultaneously visible as a dI_{SD}/dV_{SD} peak in single-hole tunnelling and a clearly sharper dI_{SD}/dV_{SD} step in inelastic co-tunnelling. As expected, the corresponding features merge at the diamond edge. The detailed field-dependence of the Zeeman splitting can be investigated by letting $B_\parallel$ (or $B_\perp$) vary at fixed V_G inside the Coulomb diamond for a spin-1/2 ground state. One such measurement is shown in Fig. 4c. The features around $B = 0$ arises from the superconductivity of the contacts. The stronger tunnel coupling in this case enables sub-gap transport based on the Andreev reflection phenomenon[38]. Above the critical field (650 and 50 mT for parallel and perpendicular fields, respectively) the spin-flip co-tunnelling steps at $eV_{SD} = \pm\Delta E_Z$ shift apart with the applied field.

To determine the full angle dependence of the g-factor, we have varied the field direction while keeping the magnitude constant at 3 T (Fig. 4d). Interestingly, the observed anisotropy does not exactly correspond to the crystal symmetry. The minimum g-factor is offset by 15–20° with respect to the parallel direction. An almost identical offset is found in another diamond for a different number of holes. The same type of data for a different device, however, shows no offset at all. We argue that the observed device dependence of the offset may originate from a generally asymmetric overlap of the metal contacts with the SiGe nanocrystal and a consequent asymmetry in the confinement potential. In principle, this asymmetry could be reduced by a controlled positioning of the contact electrodes on the SiGe nanocrystal.

Figure 4e provides an overall summary of the g-factor data obtained for five different gate voltages. Both $g_\perp$ and $g_\parallel$, and also

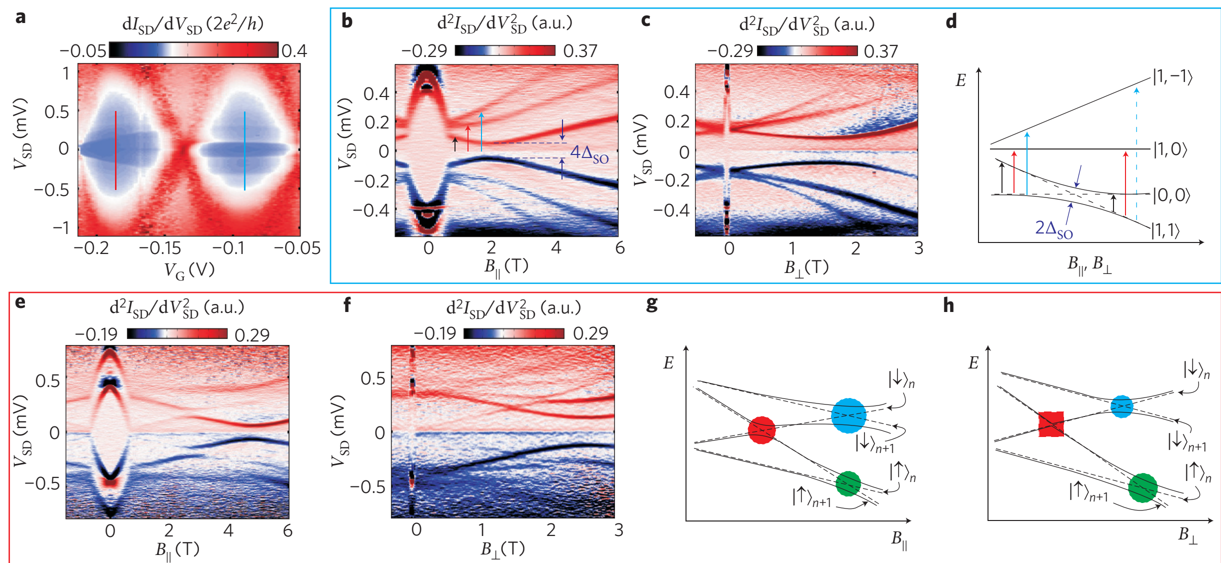

Figure 5 | Anisotropic spin–orbit coupling strength probed by inelastic co-tunnelling. **a**, False-colour plot of dI_{SD}/dV_{SD} as a function of V_G and V_{SD} at $B_\parallel = 2$ T. **b**,**c**, False-colour plots of d^2I_{SD}/dV^2_{SD} versus V_{SD} and $B_\parallel$ (**b**) and V_{SD} and $B_\perp$ (**c**) for fixed V_G at the blue line in **a**, which corresponds to an even number of confined holes. The vertical arrows in **b** indicate inelastic co-tunnelling steps for positive V_{SD}. **d**, Energy diagram showing how the spin-triplet excited state exhibits a threefold splitting in either parallel (**b**) or perpendicular magnetic fields (**c**). Owing to spin–orbit coupling, the lowest energy triplet component, |1, −1⟩, and the spin-singlet ground state, |0, 0⟩, anticross each other at $B_\parallel \approx 2$ T and $B_\perp \approx 1.5$ T. The co-tunnelling transition from |1, 1⟩ to |1, −1⟩ (dashed vertical arrow) would be forbidden in the absence of spin–orbit coupling. **e**,**f**, False-colour plots of d^2I_{SD}/dV^2_{SD} versus V_{SD} and $B_\parallel$ (**e**) and V_{SD} and $B_\perp$ (**f**) for fixed V_G at the red line in **a**, which corresponds to an odd number of confined holes. **g**,**h**, Energy diagrams illustrating the splitting of two subsequent orbital levels in parallel (**e**,**g**) and perpendicular fields (**f**,**h**). The anticrossing between opposite spin states $|\downarrow\rangle_n$ and $|\uparrow\rangle_{n+1}$ that is observed in parallel fields ($B_\parallel \approx 2.6$ T in **e**; red disk in **g**), turns into a crossing for a perpendicular field ($B_\perp \approx 1.5$ T in **f**; red square in **h**), which demonstrates a strong dependence of the spin–orbit coupling strength on the field direction. The other anticrossings (blue and green disks in **g** and **h**) might be due to purely orbital mixing.

the ratio $g_\perp/g_\parallel$, exhibit significant variations with the number of confined holes. In fact, the g-factor depends on the mixing of heavy-hole and light-hole components, which is expected to change from level to level[34] (see Supplementary Information). In addition, as the number of holes increases, the wavefunctions of the progressively occupied levels extend further into the silicon-rich base of the self-assembled nanocrystal. This should lead to an average decrease in the hole g-factor, in line with our experimental finding.

Differences in the g-factors can also be observed between ground-state and excited-state levels measured in the same charge regime, that is, at approximately the same V_G (Fig. 3e). On the other hand, the g-factors are found to be rather insensitive to V_G variations within the same Coulomb diamond. We conclude that the g-factors are clearly linked to the corresponding orbital wavefunctions, and that the latter appear to be only weakly affected by gate variations corresponding to the full width of a Coulomb diamond. Alternative gate geometries (for example, dual-gate devices) may possibly result in a more efficient g-factor tuning at a constant number of holes.

The reported values of the g-factors are obtained from a linear fit of the data in the high-field regime. In fact, an appreciable nonlinearity is found in the relation between ΔE_Z and $B_\parallel$ (or $B_\perp$), which can be seen as a field-dependent g-factor. In some cases, the g-factor can increase by as much as ∼75% for magnetic fields in the experimentally accessible range (see Fig. 4f).

Anisotropic spin–orbit coupling strength

The observed g-factor deviations from the free-particle value and the nonlinearities in the Zeeman effect constitute indirect evidence of a strong coupling between orbital and spin degrees of freedom. Although this coupling can cause spin relaxation[39] by means of the interaction with phonons, it can also provide a useful handle for coherent spin manipulation by means of gate-controlled electric fields[40–43]. To gain direct quantitative information on the SO coupling strength, we considered devices with relatively small level spacing and, incidentally, stronger tunnel couplings. A plot of dI_{SD}/dV_{SD} versus (V_G,V_{SD}) is shown in Fig. 5a for one such device at $B_\perp = 2$ T. Multiple dI_{SD}/dV_{SD} steps can be seen in two adjacent diamonds, indicating the contribution of different orbital levels to the inelastic co-tunnelling current. To identify the precise origin of these features, we fixed V_G according to the blue line in Fig. 5a and let $B_\parallel$ vary between 0 and 6 T. The result is shown in Fig. 5b, where dI_{SD}/dV_{SD} has been replaced by its numerical derivative d^2I_{SD}/dV^2_{SD} to emphasize the onset of inelastic co-tunnelling transitions.

The superconductivity-related structure around $B_\parallel = 0$ is discussed in the Supplementary Information. Above the critical field, we identify three lines which can be explained by the excitations from a spin-singlet ground state, |0, 0⟩, to three spin-triplet excited states, denoted |1, +1⟩, |1, 0⟩ and |1, −1⟩. This assignment implies an even number of confined holes. The corresponding energy diagram is qualitatively shown in Fig. 5d. The zero-field singlet–triplet splitting is ∼130 μeV. At about 2 T, an anticrossing is observed between the field-independent |0, 0⟩ state and the |1, 1⟩ state. This anticrossing between normally orthogonal states indicates the existence of mixing by means of SO coupling. An estimate of the coupling strength, Δ_{SO}, can be directly extracted from the minimum level splitting ($2\Delta_{SO}$). We find $\Delta_{SO} = 34$ μeV, which is less than an order of magnitude smaller than in InAs[44] or InSb[22] nanowires. The vertical arrows indicate the possible transitions resulting from inelastic co-tunnelling. The transition from |1, +1⟩ to |1, −1⟩, indicated by a dashed blue arrow in Fig. 5d, would be prohibited in the absence of SO coupling because it requires a change in S_z larger than 1 (ref. 45). For systems with strong SO coupling, however, states are no longer pure singlet or triplet and thus such a transition becomes possible. Similar behaviour is observed for perpendicular fields (see Fig. 5c). We also

find $\Delta_{SO} = 42$ μeV, which shows that the SO coupling strength depends on the field direction.

To further investigate this effect, we carried out the same study in the next diamond, corresponding to an odd number of holes. The observed inelastic co-tunnelling steps can be attributed to the splitting of two subsequent orbital levels with a zero-field energy difference of ~300 μeV (Fig. 5e,f). The corresponding qualitative energy diagrams are given in Fig. 5g,h, where we have indexed the spin states with the quantum numbers, n and $n+1$, of the corresponding orbitals. To obtain the best qualitative matching, we have assumed a field-induced decrease in the orbital splitting and slightly different g-factors for the two subsequent orbital levels.

An anticrossing is observed between $|\downarrow\rangle_n$ and $|\uparrow\rangle_{n+1}$ for $B_{\parallel} \approx 2.6$ T (red disk in Fig. 5g), corresponding to $\Delta_{SO} = 37$ μeV. This anticrossing turns into a crossing at $B_{\perp} \approx 1.5$ T, indicating vanishing SO coupling strength. This result is the most striking manifestation of the interplay between SO coupling and an external magnetic field, an effect that was recently predicted in a theoretical work by Golovach and colleagues for the case of GaAs quantum dots[46]. Interestingly, the observed punctual suppression of the SO coupling strength should result in a longer spin relaxation time. (During the preparation of this manuscript we have become aware that a similar anisotropy of the SO coupling strength has been observed for electrons in InAs quantum dots[47].) The other anticrossings in Fig. 5e and f cannot be used for an estimate of Δ_{SO}, because they occur between levels that could anticross even in the absence of SO coupling due to purely orbital mixing.

Outlook

The measurements of single-hole tunnelling and two-hole co-tunnelling presented here provide fresh insights into the electronic properties of self-assembled SiGe nanocrystals. We have observed finite-size quantum confinement and various effects associated with a strong and tunable SO coupling. We have also shown that it is possible to form low-resistance contacts to superconducting electrodes, and have therefore demonstrated the first example of a single-hole supercurrent transistor based on SiGe. In addition to potential device applications, self-assembled SiGe nanocrystals also provide a new versatile playground for investigating a variety of quantum phenomena in condensed matter physics. In particular, access to the strong-coupling limit could open up new opportunities to explore spin–orbit physics and other spin-related phenomena, such as the Kondo effect in combination with superconducting and possibly ferromagnetic correlations[26,27,48–50].

Received 5 February 2010; accepted 25 March 2010;
published online 2 May 2010

References

1. Javey, A., Guo, J., Wang, Q., Lundstrom, M. & Dai, H. J. Ballistic carbon nanotube field-effect transistors. *Nature* **424,** 654–657 (2003).
2. Xiang, J. *et al.* Ge/Si nanowire heterostructures as high-performance field-effect transistors. *Nature* **441,** 489–493 (2006).
3. Ryu, K. *et al.* CMOS-analogous wafer-scale nanotube-on-insulator approach for submicrometer devices and integrated circuits using aligned nanotubes. *Nano Lett.* **9,** 189–197 (2009).
4. Nam, S. W., Jiang, X., Xiong, Q., Ham, D. & Lieber C. M. Vertically integrated, three-dimensional complementary metal-oxide–semiconductor circuits. *Proc. Natl Acad. Sci. USA* **106,** 21035–21038 (2009).
5. Eaglesham, D. J. & Cerullo, M. Dislocation-free Stranski–Krastanow growth of Ge on Si(100). *Phys. Rev. Lett.* **64,** 1943–1946 (1990).
6. Mo, Y. W., Savage, D. E., Swartzenruber, B. S. & Lagally M. G. Kinetic pathway in Stranski–Krastanov growth of Ge on Si(001). *Phys. Rev. Lett.* **65,** 1020–1023 (1990).
7. Medeiros-Ribeiro, G. *et al.* Shape transition of germanium nanocrystals on a silicon (001) surface from pyramids to domes. *Science* **279,** 353–355 (1998).
8. Stangl, J., Holý, V. & Bauer, G. Structural properties of self-organized semiconductor nanostructures. *Rev. Mod. Phys.* **76,** 725–783 (2004).
9. Katsaros, G. *et al.* Kinetic origin of island intermixing during the growth of Ge on Si(001). *Phys. Rev. B* **72,** 195320 (2005).
10. Schmidt, O. G. (ed.). *Lateral Alignment of Epitaxial Quantum Dots* (Springer, 2007).
11. Katsaros, G. *et al.* Positioning of strained islands by interaction with surface nanogrooves. *Phys. Rev. Lett.* **101,** 096103 (2008).
12. Schmidt, O. G. & Eberl, K. Self-assembled Ge/Si dots for faster field effect transistors. *IEEE Trans. Electron Dev.* **48,** 1175–1179 (2001).
13. Xiang, J., Vidan, A., Tinkham, M., Westervelt, R. M. & Lieber C. M. Ge/Si nanowire mesoscopic Josephson junctions. *Nature Nanotech.* **1,** 208–213 (2006).
14. Hu, Y. A Ge/Si heterostructure nanowire-based double quantum dot with integrated charge sensor. *Nature Nanotech.* **2,** 622–625 (2007).
15. Shaji, N. *et al.* Spin blockade and lifetime-enhanced transport in a few-electron Si/SiGe double quantum dot. *Nature Phys.* **4,** 540–544 (2008).
16. Simmons, C. B. *et al.* Charge sensing and controllable tunnel coupling in a Si/SiGe double quantum dot. *Nano Lett.* **9,** 3234–3238 (2009).
17. Hayes, R. R. *et al.* Lifetime measurements (T1) of electron spins in Si/SiGe quantum dots. Preprint at http://arxiv.org/abs/0908.0173 (2009).
18. Dötsch, U. *et al.* Single-hole transistor in p-Si/SiGe quantum well. *Appl. Phys. Lett.* **78,** 341–343 (2001).
19. Petta, J. R. & Ralph, D. C. Studies of spin–orbit scattering in noble-metal nanoparticles using energy-level tunneling spectroscopy. *Phys. Rev. Lett.* **87,** 266801 (2001).
20. Winkler, R. *Spin–Orbit Coupling Effect in Two-Dimensional Electron and Hole Systems* (Springer, 2004).
21. Csonka, S. *et al.* Giant fluctuations and gate control of the g-factor in InAs nanowire quantum dots. *Nano Lett.* **8,** 3932–3935 (2008).
22. Nilson, H. A. *et al.* Giant, level-dependent g factors in InSb nanowire quantum dots. *Nano Lett.* **9,** 3151–3156 (2009).
23. Salis, G. *et al.* Electrical control of spin coherence in semiconductor nanostructures. *Nature* **414,** 619–622 (2001).
24. Roddaro, S. *et al.* Spin states of holes in Ge/Si nanowire quantum dots. *Phys. Rev. Lett.* **101,** 186802 (2008).
25. Jung, M. *et al.* Lateral electron transport through single self-assembled InAs quantum dots. *Appl. Phys. Lett.* **86,** 033106 (2005).
26. Hamaya, K. *et al.* Kondo effect in a semiconductor quantum dot coupled to ferromagnetic electrodes. *Appl. Phys. Lett.* **91,** 232105 (2007).
27. Buizert, C., Oiwa, A., Shibata, K., Hirakawa, K. & Tarucha, S. Kondo universal scaling for a quantum dot coupled to superconducting leads. *Phys. Rev. Lett.* **99,** 136806 (2007).
28. Glazman, L. I. & Matveev, K. A. Resonant Josephson current through Kondo impurities in a tunnel barrier. *JETP Lett.* **49,** 659–662 (1989).
29. Beenakker, C. W. J. & van Houten, H. Resonant Josephson current through a quantum dot, in *Single-Electron Tunneling and Mesoscopic Devices* (eds Koch, H. & Lübbig, H.) 175–179 (Springer, 1992), http://arxiv.org/abs/cond-mat/0111505.
30. Jarillo-Herrero, P., van Dam, J. A. & Kouwenhoven, L. P. Quantum supercurrent transistors in carbon nanotubes. *Nature* **439,** 953–956 (2006).
31. Cleuziou, J.-P., Wernsdorfer, W., Bouchiat, V., Ondarçuhu, T. & Monthioux, M. Carbon nanotube superconducting quantum interference device. *Nature Nanotech.* **1,** 53–59 (2006).
32. van Dam, J. A., Nazarov, Y. V., Bakkers, E. P. A. M., De Franceschi, S. & Kouwenhoven, L. P. Supercurrent reversal in quantum dots. *Nature* **442,** 667–670 (2006).
33. Winkelmann, C. B., Roch, N., Wernsdorfer, W. Bouchiat, V. & Balestro, F. Superconductivity in a single-C_{60} transistor. *Nature Phys.* **5,** 876–879 (2009).
34. Nenashev, A. V., Dvurechenskii, A. V. & Zinovieva, A. F. Wave functions and g factor of holes in Ge/Si quantum dots. *Phys. Rev. B* **67,** 205301 (2003).
35. Hensel, J. C. & Suzuki, K. Anisotropy of g factor of free hole in Ge and conduction-band spin–orbit splitting. *Phys. Rev. Lett.* **22,** 838–840 (1969).
36. Haendel, K.-M., Winkler, R., Denker, U., Schmidt, O. G. & Haug, R. J. Giant anisotropy of Zeeman splitting of quantum confined acceptors in Si/Ge. *Phys. Rev. Lett.* **96,** 086403 (2006).
37. De Franceschi, S. *et al.* Electron cotunneling in a semiconductor quantum dot. *Phys. Rev. Lett.* **86,** 878–881 (2001).
38. Buitelaar, M. R. *et al.* Multiple Andreev reflections in a carbon nanotube quantum dot. *Phys. Rev. Lett.* **91,** 057005 (2003).
39. Hanson, R., Kouwenhoven, L. P., Petta, J. R., Tarucha, S. & Vandersypen, L. M. K. Spins in few-electron quantum dots. *Rev. Mod. Phys.* **79,** 1217–1265 (2007).
40. Nitta, J., Akazaki, T., Takayanagi, H. & Enoki, T. Gate control of spin–orbit interaction in an inverted $In_{0.53}Ga_{0.47}As/In_{0.52}Al_{0.48}As$ heterostructure. *Phys. Rev. Lett.* **78,** 1335–1338 (1997).
41. Golovach, V. N., Borhani, M. & Loss, D. Electric-dipole-induced spin resonance in quantum dots. *Phys. Rev. B* **74,** 165319 (2006).
42. Nowack, K. C., Koppens, F. H. L., Nazarov, Yu. V. & Vandersypen, L. M. K. Coherent control of a single electron spin with electric fields. *Science* **318,** 1430–1433 (2007).
43. Frolov, S. M. *et al.* Ballistic spin resonance. *Nature* **458,** 868–871 (2009).
44. Fasth, C., Fuhrer, A., Samuelson, L., Golovach, V. N. & Loss, D. Direct measurement of the spin–orbit interaction in a two-electron InAs nanowire quantum dot. *Phys. Rev. Lett.* **98,** 266801 (2007).

45. Roch, N., Florens, S., Bouchiat, V., Wernsdorfer, W. & Balestro, F. Quantum phase transition in a single-molecule quantum dot. *Nature* **453,** 633–638 (2008).
46. Golovach, V. N., Khaetskii, A. & Loss, D. Spin relaxation at the singlet–triplet crossing in a quantum dot. *Phys. Rev. B* **77,** 045328 (2008).
47. Takahashi, S. *et al*. Large anisotropy of spin–orbit interaction in a single InAs self-assembled quantum dot. Preprint at http://arxiv.org/abs/0912.3088 (2009).
48. Pasupathy, A. N. *et al*. The Kondo effect in the presence of ferromagnetism. *Science* **306,** 86–89 (2004).
49. Hauptmann, J. R., Paaske, J. & Lindelof P. E. Electric-field-controlled spin reversal in a quantum dot with ferromagnetic contacts. *Nature Phys.* **4,** 373–376 (2008).
50. Zazunov, A., Egger, R., Jonckheere, T. & Martin, T. Anomalous Josephson current through a spin–orbit coupled quantum dot. *Phys. Rev. Lett.* **103,** 147004 (2009).

Acknowledgements

The authors thank T. Haccart and the PTA cleanroom team of CEA, J.-L. Thomassin and F. Gustavo for their help in device fabrication, and T. Fournier for helpful discussions and providing free access to fabrication recipes and equipment at the NANOFAB facility of the Néel Institute. We also acknowledge helpful discussions with M. Houzet, V. Golovach, W. Wernsdorfer, D. Feinberg, G. Usaj, R. Whitney, M. Sanquer, X. Jehl, G. A. Steele and E. J. H. Lee, and support from the Agence Nationale de la Recherche (through the ACCESS and COHESION projects). G.K. acknowledges further support from the Deutsche Forschungsgemeinschaft (grant no. KA 2922/1-1).

Author contributions

G.K. and S.D.F. planned the experiment, interpreted the data and co-wrote the paper. G.K. fabricated the devices, performed the measurements with P.S. and S.D.F., and analysed the data. P.S. participated in the data analysis and set up the dilution refrigerator. M.S. grew the SiGe self-assembled nanocrystal samples. F.F. fabricated the non-standard SOI wafers. M.M., V.B. and F.L. provided important help in device fabrication. A.R. and O.G.S. supervised the growth of the self-assembled SiGe nanocrystals. All authors discussed the results and commented on the manuscript.

Additional information

The authors declare no competing financial interests. Supplementary information accompanies this paper at www.nature.com/naturenanotechnology. Reprints and permission information is available online at http://npg.nature.com/reprintsandpermissions/. Correspondence and requests for materials should be addressed to G.K. and S.D.F.